Version of Record: https://www.sciencedirect.com/science/article/pii/S0169131723003654
Manuscript_17d78f708a8cbd4c3f357f5df4b5b0dc

Surface Reconstruction and Cleavage of Phyllosilicate Clay Edge by Density Functional Theory

An T. Ta[1], R. Seaton Ullberg[1], Simon R. Phillpot[1,†]

[1]Department of Materials Science and Engineering, University of Florida, Gainesville, Florida, 32611, United States

To be submitted to [Applied Clay Science]

Abstract

Phyllosilicate materials (e.g., smectite) have been proposed to act as a waste barrier within long-term deep geological repositories. Aside from longevity, these clay materials must also limit the mobility of radionuclides, which is achieved through intermolecular interaction involving clay basal planes and edge surfaces. We aim to contribute to the fundamental knowledge of clay edges by investigating surface reconstruction in a dehydrated context. Using density functional theory, surface reconstruction, charge redistribution, and formation energies have been explored for pyrophyllite edges resulting from thirteen terminations. Three primary reconstruction mechanisms were identified: (1) the displacement of Al into the tetrahedral layer, (2) proton shift, and (3) sub-surface reconstruction involving sub-surface -OH or apical O and surface Si. Reduction in overall relative bond deficiency and charge redistribution to becoming more bulk-like were found to be the main driving force for reconstruction. Formation energies were also determined with dispersion correction for dehydrated and hydrated surfaces. The presence of water terminating agents reduced energetic costs by approximately one order of magnitude and the inclusion of dispersion correction resulted in indistinguishable formation energies between different hydrated surfaces. Linear regression models were also explored to predict surface formation energies based on relative bond deficiency and charge. These models were able to identify the key contributions to the surface energy; however, due to the small dataset they were not found to be predictive.

Keywords: Clay mineral, Density functional theory, Surface formation, Edge reconstruction, Cleavage, Pyrophyllite

[†]Corresponding author: phone: 352-846-3782, email: sphil@mse.ufl.edu

1. Introduction

With a dire need for reduced carbon emissions to prevent reaching global warming thresholds (Dimitrov, 2016; Tong et al., 2019; Friedlingstein et al., 2022), nuclear energy is becoming ever more crucial as an alternative energy source to fossil fuel. To combat current climate conditions, the United States has recently become more open to new nuclear projects, for example with the inclusion of increased federal support and incentives for nuclear power in the recent Inflation Reduction Act of 2022 (*Inflation Reduction Act 2022*, 2022). The use of deep geological disposal facilities will become increasingly necessary as nuclear energy production and, hence, waste production continues and grows. As the final disposal method for radioactive high-level waste (HLW) and used nuclear fuel (UNF), geological repositories require engineered buffers to maintain their performance for long-term storage of one million years (Wall et al., 2022).

Buffer materials need to be able to protect the UNF waste package as well as to sequester harmful leaching agents in the event of container failure (Butler, 2010; Geckeis et al., 2013). For example, fission products iodine-129 and technetium-99 are major targets for capture because of their high mobility and complex chemistry in oxic environments (Meena and Arai, 2017; Zhu et al., 2017; Moore et al., 2020). Presently, all geological plans for HLW and UNF storage propose clay minerals (e.g., smectites) as their buffer material (Wall et al., 2022). The swelling capabilities of the clays are most attractive as they can expand to minimize ground water flow and prevent the waste package from corroding (Ramsay et al., 1990; Sellin and Leupin, 2013; Okada et al., 2014). Their swelling capabilities also play a crucial role in the capture of highly mobile radionuclides (Bhattacharyya and Gupta, 2008; Li et al., 2014; Carniato et al., 2020).

Clay minerals are known to possess various chemical compositions with a general form comprised of silica (SiO_4) tetrahedral (T) and alumina (AlO_6) octahedral (O) layers. Smectites are 2:1 phyllosilicates possessing a TOT layered structure and have been considered to be a strong candidate for buffer application (Wall et al., 2022). Isomorphic substitution(s) of Si^{4+} for Al^{3+}/Fe^{3+} and/or Al^{3+} for $Fe^{3+}/Mg^{2+}/Fe^{2+}$ can also occur, resulting in different molecular behaviors, including permeability. In the context of these waste applications, the importance of clay basal planes is clear. Basal planes are often recognized as key components when considering clay intercalation (Osman et al., 2003; Chang et al., 2009; Rebitski et al., 2020), water interaction (Peng et al., 2016; Ulian et al., 2021a, 2021b; Li et al., 2023), and ion adsorption (Vasconcelos et al., 2007; Lee et al., 2012; Suter et al., 2012). While not as large in surface area, edge surfaces can also interact with water (Churakov, 2007; Martins et al., 2014; Lavikainen et al., 2015), participate in ion adsorption (Strawn et al., 2004; Kremleva et al., 2015; Peng et al., 2017), and even play a role in electrochemical processes (Neumann et al., 2013). Even though both basal and edge facets can play a role in the same processes, their effect on these processes differ. Unlike basal planes, whose charge (arising from isomorphic substitution) is pH independent, the charge on edge surfaces depends on pH of the solution (White and Zelazny, 1988; Bleam et al., 1993; Tournassat et al., 2016). Undoubtedly, a complete description of the intermolecular behaviors in clay minerals requires not only an understanding of the basal but also edge facets.

The inherent control and resolution in density functional theory (DFT) calculations/simulations lend themselves well to describing the behaviors of edge surfaces. Pyrophyllite is often the preferred model for simulation studies because of its chemical simplicity and relatability to other 2:1 phyllosilicates. In this context, past simulations have been based on theoretical work by White and Zelazny (1988) and Bleam et al. (1993). White and Zelazny developed and extended the periodic bond chain theory (PBC) (Hartman and Perdok, 1955a, 1955b, 1955c) to dioctahedral 2:1 phyllosilicates (White and Zelazny, 1988). Bleam et al. (1993) later refined their model to include surface relaxation. DFT calculations have been used to aid in understanding the stabilities of various edge surfaces. Churakov (2006) performed structure/sorption studies on the (100), (010), (110), and (130) surfaces (created from an orthogonal unit cell) at low and high molecular water coverage. Differences between the surface energies were only observed at high water coverage, with the (110) and (100) edges having been reported to be the lowest in energy. Martins et al. (2014) performed a similar study but instead of an orthogonal unit cell, a conventional pyrophyllite cell was used in addition to multiple edge facets being assessed for each index surface. The (110) surface was reported to have the lowest energy. The differences between Martins et al.'s (2014) and Churakov's (2006) studies likely stem from differences in edge facets. Lavikainen et al. (2015) sought to establish more definitive trends by assessing the most likely cleavages on each lattice plane. Using an orthogonal unit cell and neutralizing broken bonds with dissociative water instead of molecular water, the (110) surface was concluded to have the lowest energy.

The presence of different edge surface groups undoubtedly creates regions that are conducive to complex chemical phenomena. DFT methods have also helped in describing the reactivity and interatomic interactions of these edge surface groups, especially in the context of pyrophyllite. Early calculations by Bickmore et al. (2003) identified the most favorable protonation schemes on the (010) and (110) pyrophyllite surfaces. Churakov (2007) later studied hydrated surface groups on (100), (010), and (110) interfaces and reported water-mediated transient proton exchanges occurring on the (010) edge. Tazi et al. (2012) dedicated efforts to describing the acidity of surface groups on the (010) facet. The ≡Si-OH groups were found to be the most acidic followed by ≡Al-OH_2, while ≡Al-OH groups did not deprotonate in water. Liu et al. (2012) sought to understand the aqueous structures/interactions of surface groups on the (010) and (110) edges. In particular, five and six-fold coordination were observed to be most stable for octahedral Al with similar energies. More recently, Forrer and Vittadini (2019) investigated the adsorption of formic acid on pyrophyllite. Their findings indicate that acid-edge chelation predominantly follows a monodentate arrangement on the (100) and (110) edges, while bidentate chelation modes is more prevalent on (100) and (130) edges. Other studies on pyrophyllite edge surfaces have also employed DFT calculations to aid atomistic simulation to understand acid activation processes (Fonseca et al., 2018), adsorbent-edge interactions, and effects of temperature (Kwon and Newton, 2016). Notably, recent computational works have started to look at edge surface behaviors in the context of smectites (Kremleva et al., 2015; Peng et al., 2016; Newton et al., 2017; Mousavi et al., 2019; Ulian et al., 2021a; Li et al., 2022; Zhao et al., 2023).

In this paper, we contribute to the understanding of complex clay surface behaviors by exploring pyrophyllite surface formation, surface charge, and underlying mechanisms in response to edge cleavage; specifically, we focus on the structure of dehydrated edges. While not generally present in equilibrium as they quickly hydrate, dehydrated surfaces offer fundamental insights into clay surface structure and to the energetics of cleavage. Surface formation energies of dehydrated and hydrated surfaces are also compared to determine the thermodynamic impact of water terminating agents on surface formation.

The rest of this paper is organized as follows. Section 2 describes the methodology of our work. Section 3 reports our results while Section 4 contains a detailed discussion of our findings which includes analyses on dehydrated cleavages, comparisons between dehydrated and hydrated cleavages, and the impact of dispersion correction methods. Section 5 concludes our work with a summary of major findings and implications. This paper is accompanied by Supplemental Information.

2. Computational model and methodology

2.1. DFT calculations

The electronic structures and atomic geometries used in this study were obtained from plane-wave density functional theory calculations via the Vienna *Ab initio* Simulation Package (VASP, v.5.4) (Kresse and Hafner, 1993; G Kresse and Furthmüller, 1996; G. Kresse and Furthmüller, 1996). Calculations were considered converged when electronic iterations and geometry optimizations reached an accuracy of 10^{-6} eV and 0.01 eV/Å, respectively. Unless noted otherwise, chemical behaviors were modeled using gradient corrected (GGA) Perdew-Burke-Ernzehof (PBE) exchange-correlation functionals (Perdew et al., 1996) in tandem with the Projector Augmented Wave (PAW) (Blochl, 1994; Kresse and Joubert, 1999) potentials. Only the valence orbitals of O, H, Al, and Si atoms were considered and a plane-wave cutoff energy of 525 eV was used. Lattice lengths were 5.18 Å x 8.99 Å x 9.28 Å and systems were sampled with a 4 x 2 x 2 Monkhorst-Pack *k*-point grid (Monkhorst and Pack, 1976). This *k*-space was chosen as it provides total energy convergence of 0.1 meV and reasonable computational efficiency (Figure S1 in Supplemental Information). Similar convergence trends were also observed during tests on edge surfaces (Figure S2 in Supplemental Information), further justifying our choice of *k*-space. Lattice parameters and average interatomic distances from those observed experimentally (Wardle and Brindley, 1972; Lee and Guggenheim, 1981) and computationally (Voora et al., 2011) in bulk pyrophyllite (see Table S1-S2 in Supplemental Information) were also reproduced using this *k*-space. Non-periodic directions in models with vacuum separation(s) were treated with a single *k*-point.

To evaluate the influence of dispersion corrections additional calculations were performed with the D3 (Grimme, 2006; Grimme et al., 2010) and vdW-DF2 (Dion et al., 2004; Lee et al., 2010) methods. These methods were chosen based on the work by Zen et al. (2016) which showed D3 having high accuracy in predicting relative adsorption energies while vdW-DF2 was superior in predicting water-clay adsorption energies. D3 and vdW-DF2 energies were taken from relaxed structures starting with configurations obtained from PBE calculations. We found this method of approach to be accurate in capturing energies while remaining moderately resource effective in our assessment of various approaches for applying the correction methods (see Supplemental Information).

2.2. Bulk and surface models for clays

Bulk pyrophyllite was constructed using a *trans*-vacant, orthogonalized ($\alpha = \beta = \gamma = 90^o$) structure with a repeating ($Al_4O_8(OH)_4$)(Si_8O_{12}) unit cell (Figure 1). Structural comparisons between the *1Tc* pyrophyllite ($C\bar{1}$ space group) and orthogonalized cells showed that bond lengths were similar (Table S2 in Supplemental Information), which indicates similar intramolecular forces. Thus, it is believed that the angle constraints will not impact chemical behaviors significantly. Calculations on systems with varying surface separations (Figure S4 in Supplemental Information) showed that surfaces needed to be at least ~12 Å apart to avoid periodic image interactions. To remain consistent throughout this study, bulk models were delaminated with a separation of ~12 Å in the (001) direction. The water model used in this study was treated as a single molecule separated by ~12 Å vacuum in each direction.

It is likely that the most probable edge surfaces will be those that involve the least number of dangling bonds and are closest to the bulk-like configuration (White and Zelazny, 1988; Bleam et al., 1993; Churakov, 2006). The most common facets for the *1Tc* pyrophyllite structure have been predicted to be the (100), (010), (110), $(\bar{1}10)$, (130), and $(\bar{1}30)$ (White and Zelazny, 1988). Due to the constrained cell geometry, the (110) and (130) facets are equivalent to the $(\bar{1}10)$and $(\bar{1}30)$, respectively, and, thus only four out of the six facets need to be considered (Churakov, 2006) (Figure 1). Based on these facets, other closely related cleavages may also be possible; some of these are symmetric, others are asymmetric. For this study, thirteen cleavages were considered (Figure 2), which have also been previously identified by Lavikainen et al. (2015).

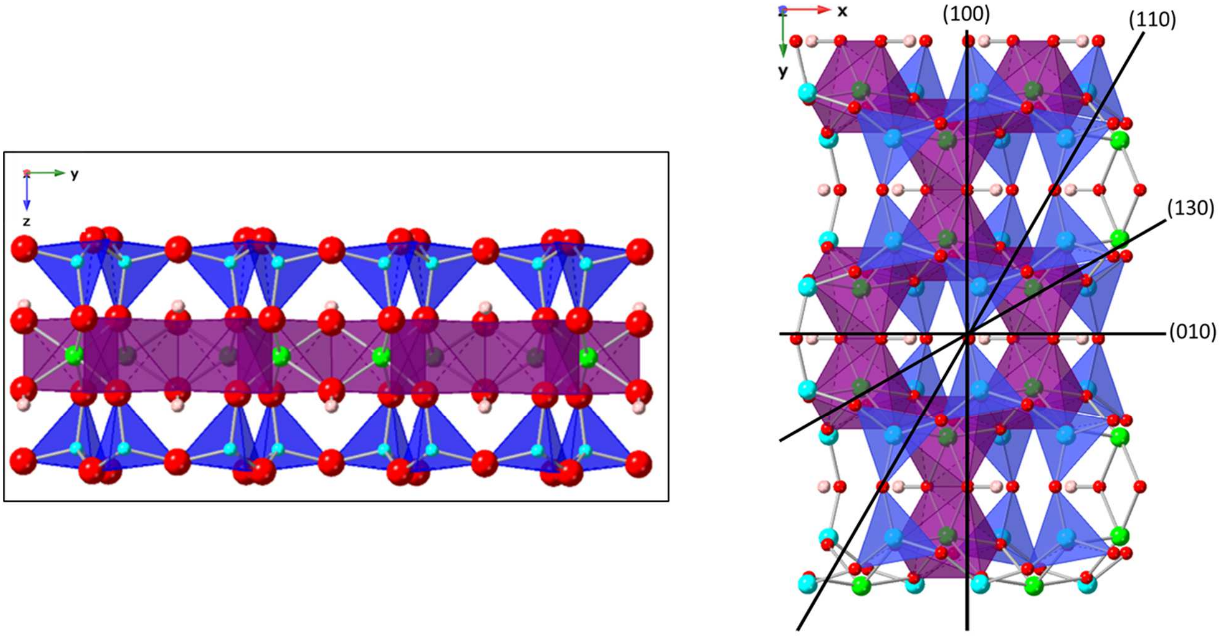

Figure 1. Side (left) and top view (right) of bulk pyrophyllite structure. Here, Si atoms are shown in blue, Al in green, oxygen in red, and hydrogen in pink. The tetrahedral and octahedral layers are also highlighted with blue and purple polyhedral, respectively. In the side view, the (100) direction is parallel to the *x* axis, the (010) direction is parallel to the *y* axis, and the (001) direction is parallel to the *z* axis. In the top view, the four planes on which pyrophyllite is cleaved are shown.

Edge models were cleaved from the bulk pyrophyllite structure as shown in Figure 2 and possessed periodic interactions in only one dimension. To avoid periodic interactions, edges and clay basal planes were separated by ~12 Å. Bulk slabs were 17.9-27.4 Å thick normal to the edges and units in the periodic direction (e.g., *y*-axis for (100), (110), and (130) or *x*-axis for (010) in Figure 2) were ~5.2 Å and ~9.0 Å for the (010)/(110) and (100)/(130) models, respectively. To avoid confusion, edge surfaces are referred to by their respective facet and suffixed with "S" for symmetrical or "A" for asymmetrical cleavages. For example, the conventional indexed surface, $(02\bar{1})$, is a symmetrical cleavage based on the (010) plane and is correspondingly referred to as the (010)S1 surface. Multiple symmetrical cuts based on the same facet are differentiated with a number as depicted in Figure 2. One structure was used to model each cleavage. For asymmetrical cuts, the left or right edge as shown in Figure 2 are donated with "α" or "β" suffixes, respectively. The conventional index planes for all considered surfaces can be found in Table S3 in Supplemental Information.

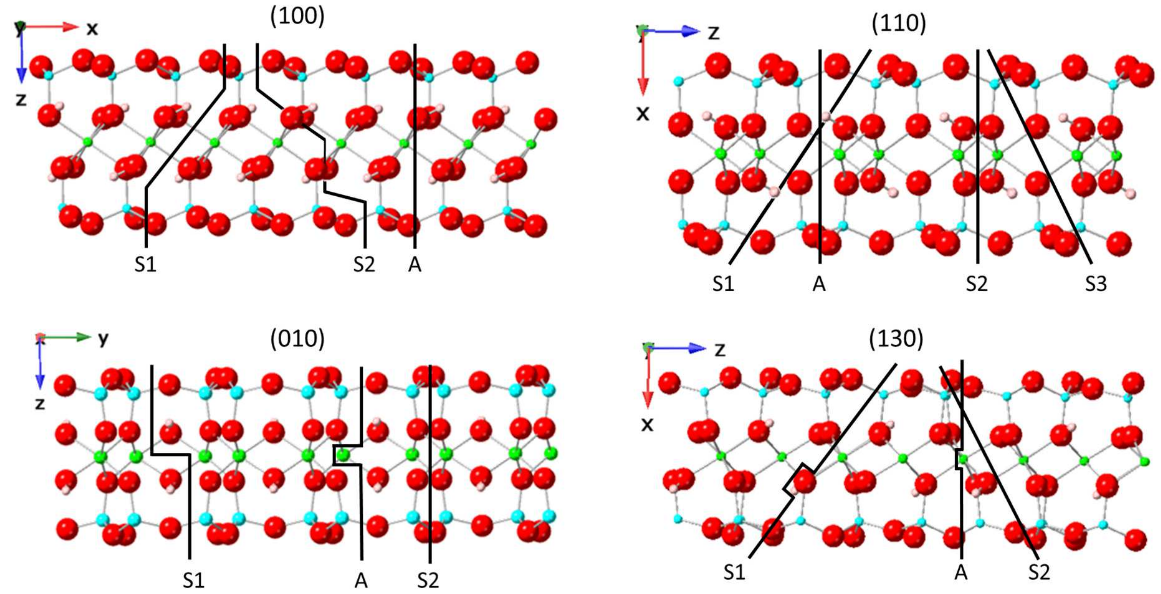

Figure 2. Cleavages investigated for each facet of pyrophyllite structure. For clarity, depicted slabs are projected onto their respective miller index plane. Cuts are labeled with "S" or "A" which denote a symmetrical or asymmetrical termination, respectively. Si atoms are shown in blue, Al in green, oxygen in red, and hydrogen in pink.

For hydrated edges, dangling bonds on surface groups were compensated via hydroxylation or protonation. The protonation and hydroxylation schemes were based on predictions from PBC theory(White and Zelazny, 1988) and are shown below:

$$\equiv Si\text{-}O^{-} \leftrightarrow \equiv Si\text{-}OH \leftrightarrow \equiv Si\text{-}OH_2^{+}$$

(1)

$$\equiv Si\text{-}O^{-\frac{1}{2}}\text{-}Al \leftrightarrow \equiv Si\text{-}OH^{+\frac{1}{2}}\text{-}Al$$

(2)

$$\equiv Al\text{-}OH^{-\frac{1}{2}} \leftrightarrow \equiv Al\text{-}OH_2^{+\frac{1}{2}} \qquad (3)$$

Notably, only half of the total number of apical O (Eq. 2) and aluminol sites (Eq. 3) need to be protonated to completely neutralize a cleaved surface. This results in several possible configurations and has been extensively assessed by Lavikainen et al. (2015) who have identified the most stable structures already. We proceed in this study using the most stable configurations reported and refer to Lavikainen et al. (2015) work for additional details. The process of bond compensation by hydroxylation/protonation results in edge surfaces being hydrated by a single layer of dissociated water. This monolayer can be understood as the principal solvation of edge atoms and is believed to have the most significant impact on surface cleavage. Consequently, our study does not account for additional layers of water beyond this monolayer.

2.3 Edge surface formation energy

In a dehydrated case, where n unit cells of pyrophyllite are terminated and produces two clay edges, the edge surface formation energy can be subsequently determined by,

$$E_{surf} = \frac{E_{edge} - nE_{bulk}}{2ab} \quad (4)$$

where E_{edge} is the total energy of the edge model, E_{bulk} is the energy of the pyrophyllite unit cell, a is the lattice length in the periodic direction, and b is the dimension of the clay slab normal to the termination plane. It is worth noting that Eq. 4 provides the surface energy for a symmetrical cut while the average energy of two distinct surfaces is given by the same equation for an asymmetrical cut. The energetic equation for a hydrated cleavage event in pyrophyllite is like the above but with additional water terms (see Supplemental Information).

2.4 Edge surface reorganization and reconstruction

To elucidate the underlying mechanisms involved with cleavage events in pyrophyllite, it is important to establish clarity on what is meant by surface reconstruction. Conventionally, surface reconstruction is considered to have occurred if the bonding/coordination environment of the edge atom(s) on the surface is different from the simple termination, typically referred to as the crystallographic surface. We follow this convention, and, in this case, the initial structures (i.e., simple termination) were the unrelaxed edge slabs while the final structures were obtained by allowing edge slabs to relax and reconstruct. For the purposes of analysis, atomic species were considered to be bonded if their separation distance was within the first coordination shell as determined via Radial Distribution Function (RDF) analyses. RDF analyses were performed for each cleavage shown in Figure 2 and the cut-off distances referenced for bond determination are reported in Table S4 in Supplemental Information.

2.5 Linear regression model

To complement the analysis of the DFT results presented in this work, a linear regression model was trained using relative partial charges and broken bond counts to predict the surface formation energy of each edge termination under investigation. More specifically, these two quantities were evaluated for each chemical species present in pyrophyllite except for hydrogen. The three unique chemical environments of oxygen (apical oxygen (O_a), basal oxygen (O_b) and hydroxyl oxygen (O_H)) were treated independently for a total of 10 parameters. During training, models using all combinations of these parameters from length 1-10 were fitted and assessed for an R^2 score. After fitting, the models were passed through a Pareto filter which was configured to retain models which maximize R^2 and minimize the number of parameters. This procedure results in 10 final models, each of which is the best performer for its respective number of parameters. More information on Pareto filters and Pareto optimality in general can be found in the Supplemental Information. Due to the small size of our dataset, R^2 values were calculated from the training set rather than a separate testing set. However, to gauge the predictive capability of these simple linear models, a cross-validation procedure was employed to assess their generalizability to unseen samples. This procedure was structured such that one sample was removed as a test case and the remaining ones were all used for training. The procedure was then replicated so that each sample was once a test case. The workflow and resulting models described above were developed in Python and rely on the *scikit-learn* (Pedregosa et al., 2011) implementation of linear regression.

3. Results

3.1 Surface reconstruction of dehydrated edges

To identify whether a reconstruction event has transpired or not, the number of bonds broken between each species (e.g., Al-Si, Si-O) were determined for the initial and final pyrophyllite structures. Strikingly, the number of broken bonds alone was found to be insufficient for identifying the occurrence of reconstruction as some processes reflected no net change in the number of broken bonds (Figure S5 in Supplemental Information). Table 1 summarizes whether a certain cleavage resulted in reconstruction as well as any corresponding mechanism(s). Three major mechanisms were identified in which surfaces experienced at least one of these processes. The first mechanism involves the displacement of Al atoms towards the tetrahedral layer and was observed for the (100)Aα, (010)Aβ, (110)S2 and (130)Aβ surfaces. Figure 3 depicts the reconstruction process in (100)Aβ and (010)Aβ, Figure 4 shows the reconstruction process in (110)S2, while (130)Aβ can be found in the Supplemental Information. In these cases, surface Al atoms shift closer to the tetrahedral layer to form a new bond with surface O_b. This reconstruction process reduces the number of broken bonds.

Table 1. Observed reconstruction processes for cleavages on the (100), (010), (110), and (130) facets of pyrophyllite. Green/shaded cells indicate that the respective process was observed.

	(100)			(010)			(110)				(130)		
reconstruction process	S1	S2	A	S1	S2	A	S1	S2	S3	A	S1	S2	A
Al displacement into T layer			🟩			🟩		🟩					🟩
proton shift between O_H and O_b	🟩					🟩				🟩			
Si reconstruction with sub-surface O_H/O_a	🟩		🟩					🟩		🟩			🟩

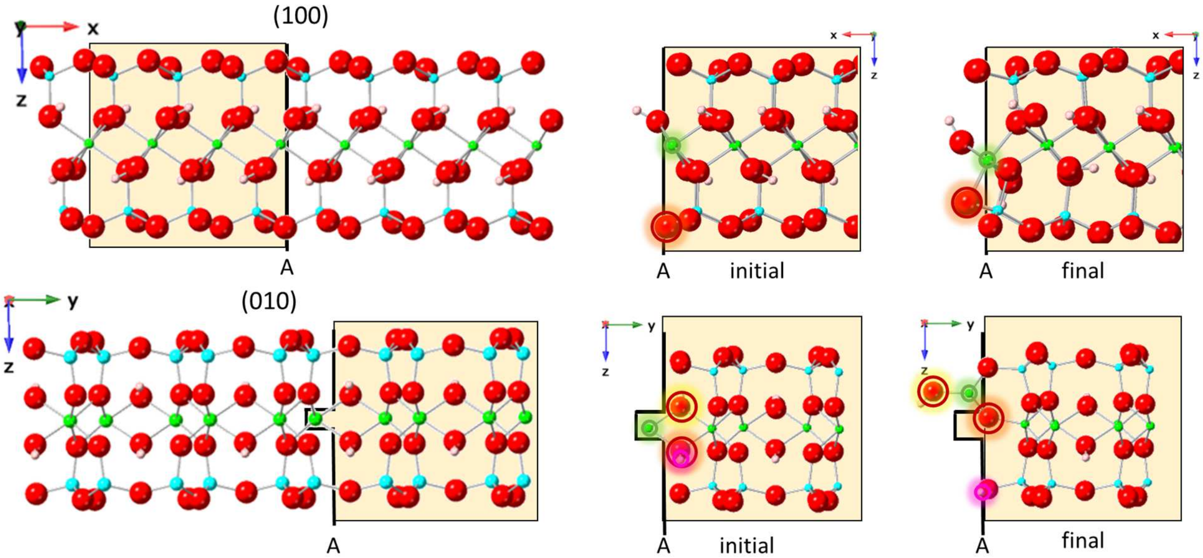

Figure 3. Edge reconstruction involving displacement of surface Al atoms into the tetrahedral layer in the (100)Aα and the (010)Aβ surfaces. For clarity, atoms that participate in reconstruction are circled/highlighted in the initial and final edge structures. Note that the

(010)Aβ surface also contains a proton shift mechanism (circle/highlighted in pink). Si atoms are shown in blue, Al in green, oxygen in red, and hydrogen in pink.

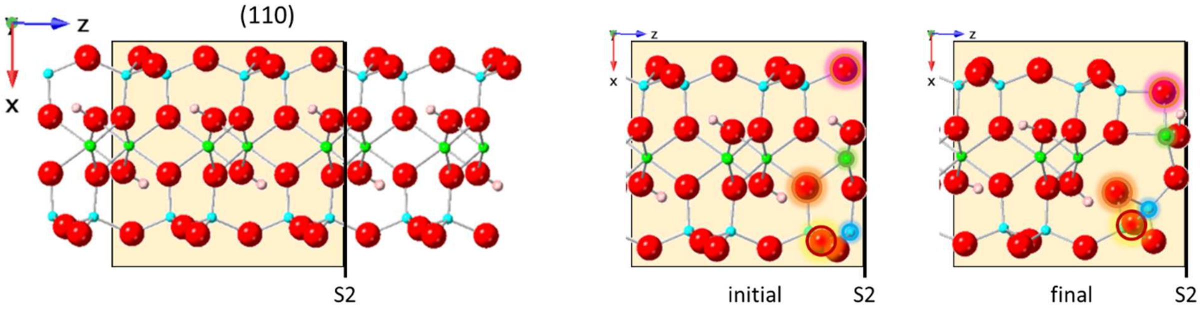

Figure 4. Edge reconstruction involving Al displacement and sub-surface reconstruction involving O_a in (110)S2. For clarity, atoms that participate in reconstruction are circled/highlighted in the initial and final edge structures. Si atoms are shown in blue, Al in green, oxygen in red, and hydrogen in pink.

The second major process involves a proton shift between O_H and O_b atoms, which was observed for the (100)S1, (010)Aβ, and (110)Aβ surfaces. Figures 3 and 5 show (010)Aβ and (100)S1 surfaces, respectively, while (110)Aβ can be found in the Supplemental Information. Specifically, the O_H atoms in the tetrahedral layer lost their proton to a neighboring O_b in the octahedral layer. These proton transfer mechanisms alone do not reflect any changes in the number of broken bonds on edge surfaces.

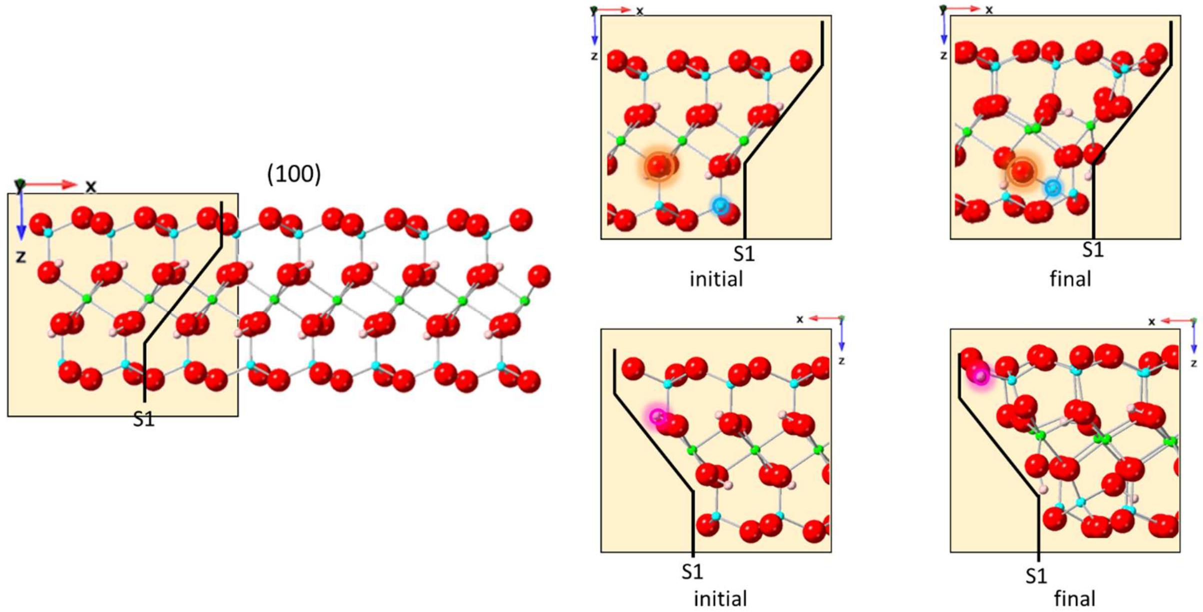

Figure 5. Edge reconstruction involving sub-surface reorganization (top) between surface Si and sub-surface O_H and proton shift (bottom) on (100)S1. For clarity, atoms that participate in

reconstruction are circled/highlighted in the initial and final edge structures. Si atoms are shown in blue, Al in green, oxygen in red, and hydrogen in pink.

The third process involves reconstruction in which surface Si and sub-surface O shift to form bonds with one another. The surfaces that observed this reconstruction include the (100)S1, (100)Aβ, (110)Aα, (110)S2, and (130)Aα. The edge reconstruction for the (100)S1 (shown in Figure 5), (100)Aβ, (110)Aα, and (130)Aα (shown in the Supplemental Information to avoid redundancy) involves the displacement of a sub-surface $O_{H.}$ Surface Si was observed to be pulled in closer to the bulk while sub-surface O_H was displaced closer to the surface such that the pair formed a bond with one another.

While most sub-surface processes were observed to primarily involve O_H atoms, the O_a atoms may also participate in this type of reconstruction mechanism. A visual account of edge reconstruction involving sub-surface O_a can be observed from Figure 4 on the (110)S2 surface. It is worth noting that the Al originally coordinating with the sub-surface O_H/O_a loses its bond to that respective O in this process which results in a coordination deficiency that it did not have before. The sub-surface processes will not reflect a change in the number of broken bonds in edge surfaces.

3.2 Bader charge distribution of dehydrated edges

Bader charge analyses were also performed on surface atoms to better understand the impact of cleavages and edge reconstruction. Using bulk pyrophyllite as a reference, the partial charge of surface atoms was monitored to quantifiably evaluate changes in electronic behavior. By taking the difference in partial charges of surface atoms relative to their bulk counterparts, a charge map can be created to visualize the charge distribution on edge surfaces. After reconstruction with Al displacement towards the tetrahedral layer, the newly formed bonds between Al and O_b help re-distribute the high charge density on surface Al to O_b. Figure 6 and 7 shows the charge map for surface atoms in (100)Aβ/(010)Aβ and (110)S2, respectively. It can be observed that the Al atom on the surface was initially more negatively charged while the corresponding O_b was more positive than their bulk counterparts. After reconstruction, the negative/positive charge on Al/O_b were observed to redistribute, presumably to one another and both atoms were observed to have charges more like their bulk counterparts. The charge redistribution for the (130)Aβ surface was also similar and is shown in the Supplemental Information.

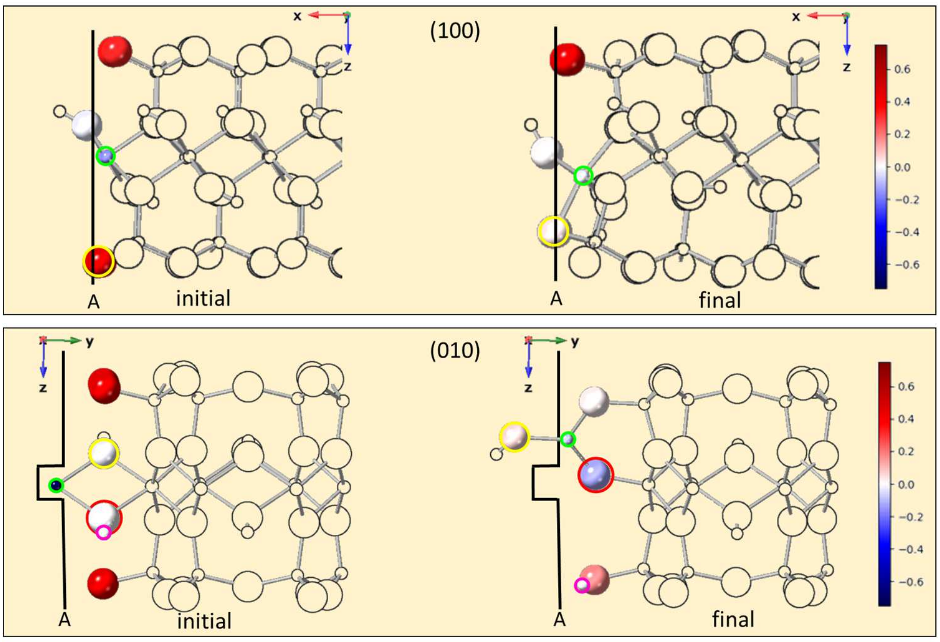

Figure 6. Charge map of the initial and final edges of the (100)Aβ and (010)Aβ surfaces. Color gradient denotes the difference between the charge of the atoms relative to their bulk counterparts and is only shown for surface atoms for clarity. Atoms that participate in reconstruction are also circled. Note that the perspective shown is the same as that shown in Figure 3.

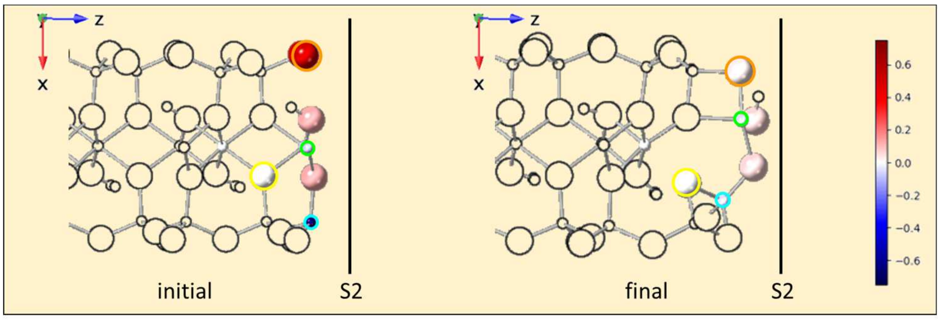

Figure 7. Charge map of the initial and final edges of (110)S2 surface. Color gradient denotes the difference between the charge of the atoms relative to their bulk counterparts and is only shown for surface atoms and those involved in reconstruction for clarity. Atoms that participate in reconstruction are also circled. Note that the perspective shown is the same as that shown in Figure 4.

Charge re-distribution from the proton shift process in the (010)Aβ and (100)S1 surfaces are shown in Figure 6 and 8, respectively. Surface O_b atoms in the (010)Aβ/(100)S1 were also observed to have a more positive charge initially. After receiving a proton from a neighboring O_H, O_b atoms gained some electronic charge, albeit with a relatively higher positive charge after reconstruction. The re-distribution of charge for the corresponding O_H was also similar in the (010)Aβ and (100)S1 surfaces. It can be observed in Figure 6 and 8 that the O_H atom became slightly more negative.

The changes in charge distribution when sub-surface reconstruction occurs are shown in Figure 7 and 8 for the (110)S2 and (100)S1 surfaces, respectively. Similar redistribution was observed in both cases of either subsurface O_a (Figure 7) or O_H (Figure 8) participating in the reconstruction process. Surface Si initially possessed a more negative charge than its bulk counterparts but was able to lower its relatively high charge concentration following reconstruction. Meanwhile the sub-surface O_a/O_H and Al (lost one bond after reconstruction) possessed similar charges before and after reconstruction.

Charge distributions becoming more like their bulk counterparts is also evidenced when considering the sum of absolute relative partial charges in the initial and final structures. From Figure 9, edge surfaces that were most like bulk pyrophyllite were consistently those that underwent reconstruction in each facet group (Figure 2). Nearly all edge structures experienced some reduction in charge discrepancy between the surface and bulk atoms regardless of having reconstructed or not. The (110)S3 surface was the only exception to this which is likely due to it being amongst one of the most energetically expensive terminations while also having a relatively high number of broken bonds (Figure 10).

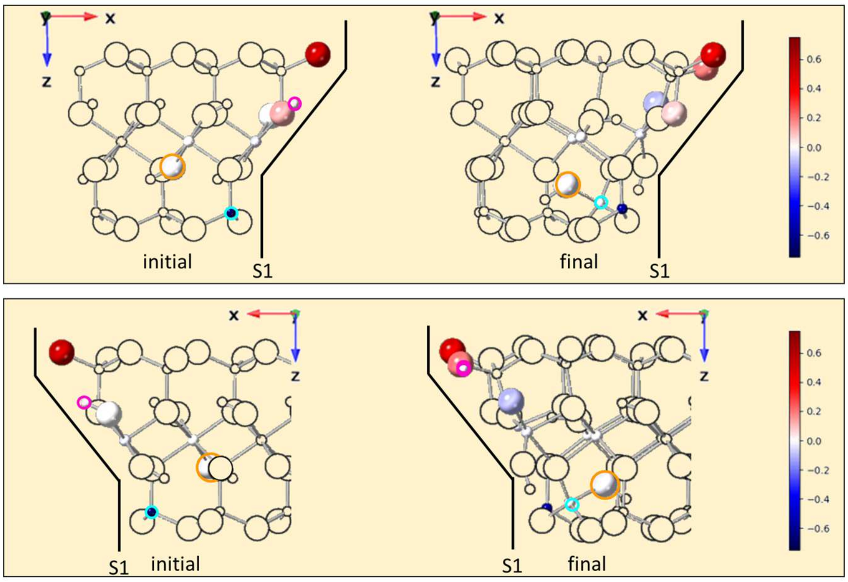

Figure 8. Charge map of the initial and final edges of (100)S1 surface from two different perspectives. Color gradient denotes the difference between the charge of the atoms relative to their bulk counterparts and is only shown for surface atoms and those involved in reconstruction for clarity. Atoms that participate in reconstruction are also circled. Note that the perspective shown is the same as that shown in Figure 5.

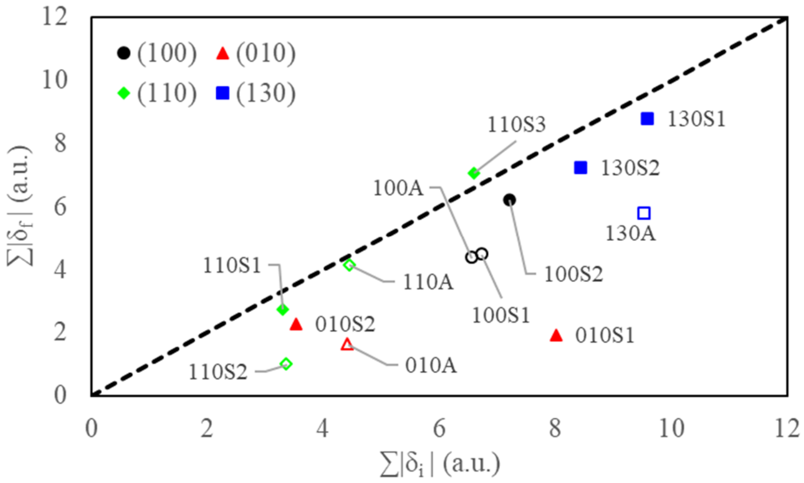

Figure 9. Sum of relative charge of atoms in the final versus initial edge structures. Open symbols denote surfaces that underwent reconstruction and points below the dashed line denote a decrease in differences in charge distribution of edge structure atoms and bulk pyrophyllite.

3.3 Edge surface formation energies

Surface formation energies obtained using D3 and vdWDF2 are shown in Figure 10. For dehydrated structures, the lowest formation energies were found to correspond to surfaces that underwent surface reconstruction: (110)S2 < (010)A < (100)A. For hydrated surfaces, dispersion corrected energies were less distinct from one another and four surfaces were observed to be most probable: (100)S1 ≈ (010)S2 ≈ (110)S1 ≈ (130)S2. Notably, relative formation energies are slightly more distinct for vdwDF2, albeit not enough to claim a dominant surface. Thermodynamic impact of water terminating agents was also found by comparing energies between dehydrated and hydrated surfaces. The presence of water lowered the surface formation energies by ~74-89% in magnitude (tabulated formation energies are reported in Supplemental Information).

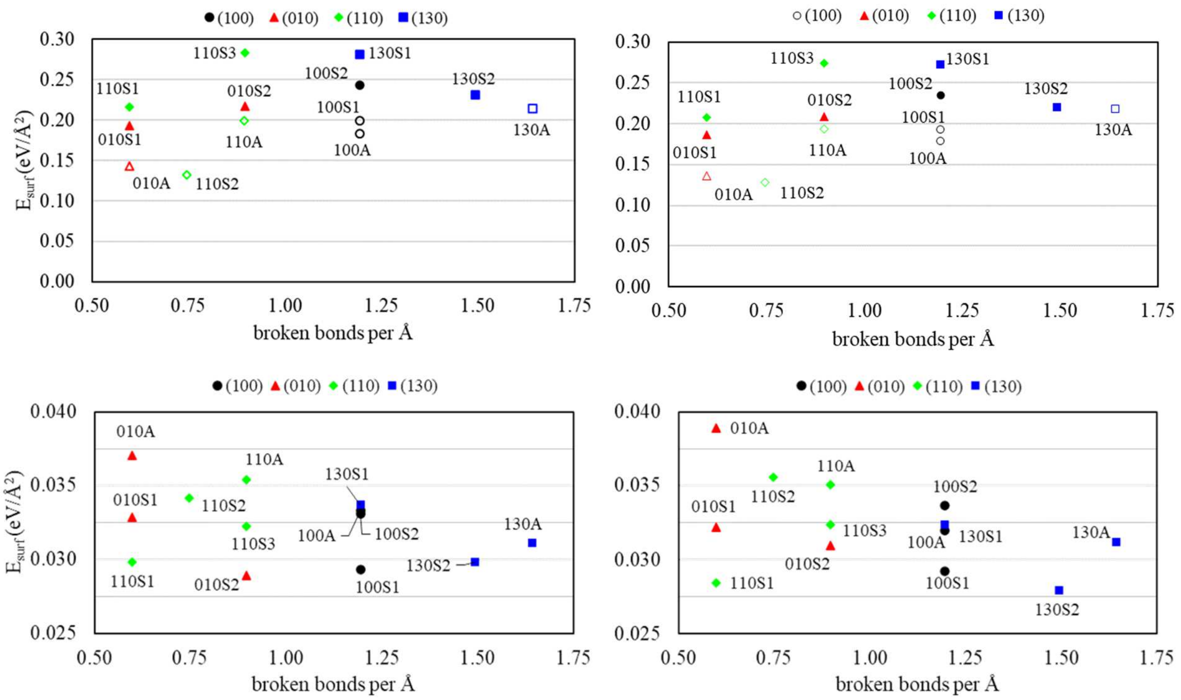

Figure 10. Surface formation energies calculated with D3 (left) and vdWDF2 (right) dispersion correction methods for dehydrated (top row) and hydrated (bottom row) edges as a function of broken bonds per Ångstrom. Open symbols denote surfaces that underwent reconstruction.

3.4 Linear regression model

Parity plots depicting the performance of linear regression models trained to predict the final (i.e., relaxed or reconstructed) surface formation energy of unrelaxed and relaxed edge surface structures are shown in Figure 11. As described in Section 2.5, multiple models were fitted using all possible combinations of input parameters and efficient models were selected using a Pareto filter. Analysis of the mean squared error (MSE) for each model indicates that the best model trained on the relaxed dataset outperforms the best model trained on the unrelaxed dataset by a factor of 2. Additionally, we find that the best performing model trained on the unrelaxed dataset is a 7-parameter model consisting of Al, O_a, and O_H charges and Al, O_b, O_a, and O_H broken bonds. The best performing model trained on the relaxed dataset is a simple 2-parameter model consisting of only Si partial charge and O_a broken bonds. As a direct comparison, we also evaluated the loss function for a model using just Si partial charge and O_a broken bonds (the best parameters for the relaxed dataset) on the unrelaxed dataset and find that it performs 3.5x worse than the model trained using the relaxed parameters. These findings indicate that the models can be rapidly overfit to the dataset which is the expected behavior for small datasets.

To better understand how each parameter is contributing to the overall surface formation energy, we counted the frequency with which each parameter was found in the parameter set of a Pareto efficient model. A parameter can be counted a maximum of 10 times (occurring in every model), or a minimum of 1 (only being included in the full model). Using this schema, the surface formation energy can be interpreted as being sensitive to parameters which occur most often and relatively insensitive to those which are less common. We find that for the unrelaxed dataset there are four parameters which occur in 7 of the maximum 10 models. Those parameters are Si and O_a partial charges and Al and O_a broken bonds. The least common parameter for the unrelaxed dataset is O_b partial charges which only occurred in 3 Pareto efficient models. In the models trained on the relaxed dataset, Si partial charges were present in every Pareto efficient model indicating a very high sensitivity to this parameter. O_H partial charges was the least common parameter occurring in only 3 of the possible 10 models. A full tabulation of MSE and parameter sets for each model is presented in the Supplemental Information.

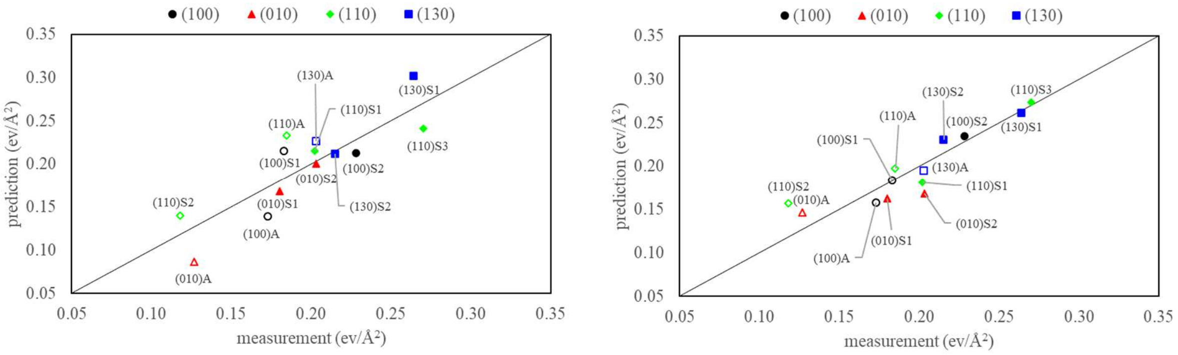

Figure 11. Parity plots illustrating the predictive performance of the best linear regression model trained on data from the unrelaxed edge structures (left) and edge structures which underwent geometric relaxation (right). Open symbols denote surfaces that underwent reconstruction.

4. Discussion

4.1 Edge surface reconstruction

To explain the reconstruction process discussed in Section 3.1 and 3.2, two approaches can be taken: (1) discussion based on relative coordination and (2) discussion based on charge distribution. With the former, it is important to consider the different bond deficiencies experienced by surface atoms after a cleavage event. Relative to the bulk crystallographic structure, the loss of one bond by Si results in a relative deficiency of -25% (bulk bonds = 4), for O_b this deficiency equates to -50% (bulk bonds = 2), for O_H or O_a the deficiency is -33% (bulk bonds = 3) and for Al its deficiency experience is -16.7% (bulk bonds = 6). If a bond is lost due to cleavage and reconstruction is feasible, surface atoms typically shift to compensate for broken bonds. In the simplest case, a complete reduction in deficiency is observed and, in turn, a decrease in the total number of broken bonds is achieved following reconstruction. For example, Al displacement towards the tetrahedral layer results in the recovery of bonds by surface Al and O_b atoms. This displacement allowed for the pair to recover one lost bond each by forming an Al-O_b bond, resulting in a reduced bond deficiency of -33→-16.7% and -50→0% for Al and O_b, respectively.

To understand processes that do not involve a change in the total number of broken bonds, a comprehensive consideration of bond deficiencies is required. Figure 12 provides a visual of the overall bond deficiencies between initial and final surface structures. Considering the proton shift in the (010)Aβ and the (100)S1 surfaces, the O_H that gave up its H atom experienced an increase in bond deficiency while O_b experienced a decrease due to the newly formed H-O_b bond. The difference between the two changes is still considered favorable because they result in a net reduction of -17% in relative bond deficiency (Figure 12). Particularly, the change in deficiencies were 0→-33% and -50→0% for the O_H and O_b, respectively.

Sub-surface reconstruction can also be explained through relative deficiency. During this process, Si and sub-surface O_H/O_a form a Si-O bond but sub-surface Al loses its bond with that respective O atom. Typically, the O_a/O_H makes up any loss in coordination with Al by forming a new bond with Si – a 1:1 pair exchange. The change in relative deficiency experienced by Si is -25→0%, sub-surface Al is 0→-16.7%, and the O_a/O_H does not experience a change in bond number which corresponds to a net decrease in deficiency.

The (100)S1 surface was an exception to the 1:1 pair exchange and its reconstruction mechanism resulted in a slight increase in net bond deficiency (Figure 5). In this case, sub-surface O_H atom lost its bond with two Al atoms while only gaining one with surface Si (a different viewpoint of the reconstruction is provided in the Supplemental Information). While counterintuitive from the perspective of relative coordination, the favorability for this reconstruction is apparent in Figure 8 and 9 which shows that the slight sacrifice in bonding resulted in charge distributions that were more bulk-like. This precedence in the (100)S1 also suggests that charge distribution can act as a stronger driving force for reconstruction than bond recovery.

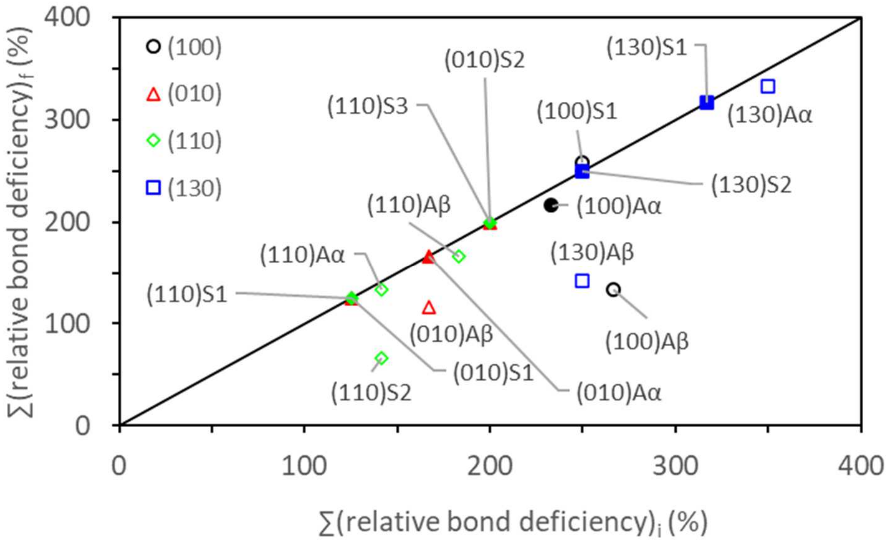

Figure 12. Sum of relative bond deficiencies of atoms found in the final versus the initial surface structures that underwent reconstruction. A net reduction in bond deficiency results in data points being beneath the black line. Open symbols denote surfaces that underwent reconstruction.

The bulk charge difference can also reflect the respective atoms relative bond deficiency. For example, in Figures 6-8, surface Al atoms that lost one bond (deficiency = -16.7%) was observed to have similar charge distribution as their bulk counterparts as opposed to surface Si atoms that lost one bond (deficiency = -25%). Moreover, surface atoms were observed to redistribute their charge density (if possible) to be more like their bulk counterparts as evidenced in Figure 9.

4.2 Edge surface formation energies

The small differences between D3 and vdWDF2 formation energies implies that the two correction methods are substantially equivalent in the application of modeling phyllosilicates. Modelling dehydrated and hydrated surfaces also allowed for the isolation of thermodynamic impact of water terminating agents which was found to lower the energy cost for surface formation by an order of magnitude. Furthermore, the inclusion of dispersion methods showed that the formation energies between different edges were indistinguishably small for the hydrated edges. Previous studies by Martins *et al.* (2014) also exhibited similar qualitative contrast between edges with adsorbed molecular water using D2 correction methods (Martins et al., 2014). Our work and that reported by Martins *et al.* (2014) collectively points to a likelihood of heterogenous surface formation in phyllosilicates.

4.3 Linear regression model

In the context of this work, the models presented in Figure 11 are more applicative as descriptive tools rather than predictive ones. Figures 9 and 12 illustrate the complementary influence of relative partial charge and relative bond deficiency respectively, but they cannot describe which of these properties dominates or how they interact. Creating an ensemble of linear models as we have done in this work allows us to quantitatively inspect, through analysis of the MSE, which parameters are most closely correlated with surface formation energy. Most notably, we find that surface formation energy can be predicted within an error of 0.038 eV/Å^2 using only the relative partial charge of Si and the broken bonds of O*a*. This suggests that these two factors are crucial in controlling the surface formation energy of a pyrophyllite sheet. It is worth noting that partial charges and broken bonds are represented in the best performing model, which suggests that both partial charges and broken bonds are required for a full picture of the thermodynamics of edge surface formation.

5. Conclusion

Surface reconstruction for various dehydrated pyrophyllite edges were investigated using DFT. Our study focused on seventeen unique surfaces that were generated based off of the most common facets for *1Tc* pyrophyllite (White and Zelazny, 1988; Lavikainen et al., 2015). Three primary reconstruction mechanisms were identified in which a surface experienced at least one of these processes: (1) Al displacement into the T layer, (2) proton shift between O_H and O_b, and (3) Si reconstruction with sub-surface O_H/O_a.

The understanding of surface reconstruction in clay materials requires two key perspectives. Firstly, the relative bond deficiency, such as a 50% deficiency resulting from the loss of one bond by O_b, is a crucial factor in describing the driving force behind reconstruction. Most observed reconstruction processes resulted in a reduction in relative bond deficiency. Secondly, Bader charge analyses underscore the prominence of charge distribution as a driving force for these processes. Reconstruction consistently involves minimizing disparities in charge distribution of surface and bulk atoms across all processes observed in this study.

Surface formation energies for dehydrated and hydrated edges were predicted using D3 and vdWDF2 corrections. The methods showed consistent results, suggesting their equivalent performance in modeling phyllosilicates. Comparing these surfaces isolates the energetic impact of water presence, revealing a tenfold reduction in energy cost when a water terminating agent is present.

Linear regression models using relative partial charges and relative bond deficiencies were trained to explore their potential to predict surface formation energies. These models offer valuable insights into the interplay between relative partial charge and relative bond deficiency, but their predictive performance is limited by the dataset's size. They perform poorly on unrelaxed surfaces, making them ineffective for predictions. When trained on unrelaxed surfaces, significant contributors to surface formation energy include O_a and Si partial charges, as well as Al and O_a broken bonds. In contrast, predictions from relaxed surface data emphasize Si partial charges. The best performing model incorporates both partial charges and broken bond parameters, suggesting their joint importance for describing edge surface formation energies comprehensively.

By leveraging DFT, we were able to resolve fundamental processes intrinsic to phyllosilicate and their response to termination/cleavage. The work herein studied cases of dehydrated surfaces and can therefore serve as a reference for future work involved with clay surface behaviors and their edge interactions with relevant adsorbent species. The development and use of linear regression models, although admittedly trained on a small dataset, also illustrates the usefulness of machine learning to further understand and identify properties that may have the strongest impact on the thermodynamics of surface formation.

Acknowledgements

The authors would like to thank Nathalie A. Wall (University of Florida), Emily Maulden (University of Florida), Elizabeth J. Gager (University of Florida), Juan C. Nino (University of Florida), Carolyn I. Pearce (PNNL), James E. Szecsody (PNNL) for their invaluable insight and conversations pertaining to this study. We also acknowledge University of Florida Research Computing for providing computational resources and support.

Data Availability

Essentially all data is contained in this manuscript and Supplemental Information, though, additional data can be available on reasonable request.

Funding

This work was supported by U.S. DOE Office of Nuclear Energy's Nuclear Energy University Program under grant DE-NE0008952.

Notes

The authors declare no competing financial interest.

References

Bhattacharyya, K.G., Gupta, S. Sen, 2008. Adsorption of a few heavy metals on natural and modified kaolinite and montmorillonite: A review. Adv. Colloid Interface Sci. https://doi.org/10.1016/j.cis.2007.12.008

Bickmore, B.R., Rosso, K.M., Nagy, K.L., Cygan, R.T., Tadanier, C.J., 2003. Ab initio determination of edge surface structures for dioctahedral 2:1 phyli-osilicates: Implications for acid-base reactivity. Clays Clay Miner. 51, 359–371. https://doi.org/10.1346/CCMN.2003.0510401

Bleam, W.F., Welhouse, G.J., Janowiak, M.A., 1993. The surface Coulomb energy and proton Coulomb potentials of pyrophyllite {010}, {110}, {100}, and {130} edges. Clays Clay Miner. 41, 305–316. https://doi.org/10.1346/CCMN.1993.0410305

Blochl, P.E., 1994. Projector augmented-wave method. Phys. Rev. B 50, 17953–17979. https://doi.org/https://doi.org/10.1103/PhysRevB.50.17953

Butler, D., 2010. France Digs Deep for Nuclear Waste. Nature 466, 804–805.

Carniato, F., Gatti, G., Bisio, C., 2020. An overview of the recent synthesis and functionalization methods of saponite clay. New J. Chem. 44, 9969–9980. https://doi.org/10.1039/d0nj00253d

Chang, P.H., Li, Z., Jiang, W.T., Jean, J.S., 2009. Adsorption and intercalation of tetracycline by swelling clay minerals. Appl. Clay Sci. 46, 27–36. https://doi.org/10.1016/j.clay.2009.07.002

Churakov, S. V., 2007. Structure and dynamics of the water films confined between edges of pyrophyllite: A first principle study. Geochim. Cosmochim. Acta 71, 1130–1144. https://doi.org/10.1016/j.gca.2006.11.026

Churakov, S. V., 2006. Ab initio study of sorption on pyrophyllite: Structure and acidity of the edge sites. J. Phys. Chem. B 110, 4135–4146. https://doi.org/10.1021/jp053874m

Dimitrov, R.S., 2016. The Paris agreement on climate change: Behind closed doors. Glob. Environ. Polit. 16, 1–11. https://doi.org/10.1162/GLEP_a_00361

Dion, M., Rydberg, H., Schröder, E., Langreth, D.C., Lundqvist, B.I., 2004. Van der Waals density functional for general geometries. Phys. Rev. Lett. 92, 246401. https://doi.org/10.1103/PhysRevLett.92.246401

Fonseca, C.G., Vaiss, V.S., Wypych, F., Diniz, R., Leitão, A.A., 2018. Investigation of the initial stages of the montmorillonite acid-activation process using DFT calculations. Appl. Clay Sci. 165, 170–178. https://doi.org/10.1016/j.clay.2018.08.012

Forrer, D., Vittadini, A., 2019. A DFT-D2 study of formic acid adsorption at smectite edges based on pyrophyllite models. Chem. Phys. Lett. 733, 136687. https://doi.org/10.1016/j.cplett.2019.136687

Friedlingstein, P., O'Sullivan, M., Jones, M.W., Andrew, R.M., Gregor, L., Hauck, J., Le Quéré, C., Luijkx, I.T., Olsen, A., Peters, G.P., Peters, W., Pongratz, J., Schwingshackl, C., Sitch, S., Canadell, J.G., Ciais, P., Jackson, R.B., Alin, S.R., Alkama, R., Arneth, A., Arora, V.K., Bates, N.R., Becker, M., Bellouin, N., Bittig, H.C., Bopp, L., Chevallier, F., Chini, L.P., Cronin, M., Evans, W., Falk, S., Feely, R.A., Gasser, T., Gehlen, M., Gkritzalis, T., Gloege, L., Grassi, G., Gruber, N., Gürses, Ö., Harris, I., Hefner, M., Houghton, R.A., Hurtt, G.C., Iida, Y., Ilyina, T., Jain, A.K., Jersild, A., Kadono, K., Kato, E., Kennedy, D., Klein Goldewijk, K., Knauer, J., Korsbakken, J.I., Landschützer, P., Lefèvre, N., Lindsay, K., Liu, J., Liu, Z., Marland, G., Mayot, N., McGrath, M.J., Metzl, N., Monacci, N.M., Munro, D.R., Nakaoka, S.-I., Niwa, Y., O'Brien, K., Ono, T., Palmer, P.I., Pan, N., Pierrot, D., Pocock, K., Poulter, B., Resplandy, L., Robertson, E., Rödenbeck, C., Rodriguez, C., Rosan, T.M., Schwinger, J., Séférian, R., Shutler, J.D., Skjelvan, I., Steinhoff, T., Sun, Q., Sutton, A.J., Sweeney, C., Takao, S., Tanhua, T., Tans, P.P., Tian, X., Tian, H., Tilbrook, B., Tsujino, H., Tubiello, F., van der Werf, G.R., Walker, A.P., Wanninkhof, R., Whitehead, C., Willstrand Wranne, A., Wright, R., Yuan, W., Yue, C., Yue, X., Zaehle, S., Zeng, J., Zheng, B., 2022. Global Carbon Budget 2022. Earth Syst. Sci. Data 14, 4811–4900. https://doi.org/10.5194/essd-14-4811-2022

Geckeis, H., Lützenkirchen, J., Polly, R., Rabung, T., Schmidt, M., 2013. Mineral-water interface reactions of actinides. Chem. Rev. 113, 1016–1062. https://doi.org/10.1021/cr300370h

Grimme, S., 2006. Semiempirical GGA-type density functional constructed with a long-range dispersion correction. J. Comput. Chem. 27, 1787–1799. https://doi.org/10.1002/jcc.20495

Grimme, S., Antony, J., Ehrlich, S., Krieg, H., 2010. A consistent and accurate ab initio parametrization of density functional dispersion correction (DFT-D) for the 94 elements H-Pu. J. Chem. Phys. 132, 24109. https://doi.org/10.1063/1.3382344

Hartman, P., Perdok, W.G., 1955a. On the Relations Between Structure and Morphology of Crystals. I. Acta Crystallogr. 8, 49–52. https://doi.org/10.1016/0022-0248(91)90646-M

Hartman, P., Perdok, W.G., 1955b. On the Relations Between Structure and Morphology of Crystals. II. Acta Crystallogr. 8, 521–524.

Hartman, P., Perdok, W.G., 1955c. On the Relations Between Structure and Morphology of Crystals. III. Acta Crystallogr. 8, 525–529.

Inflation Reduction Act 2022, 2022. . 117th Congress of U.S., Pub.L. 117-169.

Kremleva, A., Krüger, S., Rösch, N., 2015. Uranyl adsorption at solvated edge surfaces of 2:1 smectites. A density functional study. Phys. Chem. Chem. Phys. 17, 13757–13768. https://doi.org/10.1039/c5cp01074h

Kresse, G, Furthmüller, J., 1996. Efficient iterative schemes for ab initio total-energy calculations using a plane-wave basis set. Phys. Rev. B - Condens. Matter Mater. Phys. 54, 11169–11186. https://doi.org/10.1103/PhysRevB.54.11169

Kresse, G., Furthmüller, J., 1996. Efficiency of ab-initio total energy calculations for metals and semiconductors using a plane-wave basis set. Comput. Mater. Sci. 6, 15–50.

https://doi.org/10.1016/0927-0256(96)00008-0

Kresse, G., Hafner, J., 1993. Ab initio molecular dynamics for liquid metals. Phys. Rev. B 47, 558–561. https://doi.org/10.1016/0022-3093(95)00355-X

Kresse, G., Joubert, D., 1999. From ultrasoft pseudopotentials to the projector augmented-wave method. Phys. Rev. B 59, 1758–1775. https://doi.org/10.1103/PhysRevB.59.1758

Kwon, K.D., Newton, A.G., 2016. Structure and stability of pyrophyllite edge surfaces: Effect of temperature and water chemical potential. Geochim. Cosmochim. Acta 190, 100–114. https://doi.org/10.1016/j.gca.2016.06.021

Lavikainen, L.P., Hirvi, J.T., Kasa, S., Schatz, T., Pakkanen, T.A., 2015. Stability of dioctahedral 2:1 phyllosilicate edge structures based on pyrophyllite models. Theor. Chem. Acc. 134, 112. https://doi.org/10.1007/s00214-015-1715-6

Lee, J.H., Guggenheim, S., 1981. Single-crystal X-ray refinement of pyrophyllite-1Tc. Am. Mineral. 66, 350–357.

Lee, K., Murray, É.D., Kong, L., Lundqvist, B.I., Langreth, D.C., 2010. Higher-accuracy van der Waals density functional. Phys. Rev. B - Condens. Matter Mater. Phys. 82, 081101. https://doi.org/10.1103/PhysRevB.82.081101

Lee, S.S., Fenter, P., Nagy, K.L., Sturchio, N.C., 2012. Monovalent ion adsorption at the muscovite (001)-solution interface: Relationships among ion coverage and speciation, interfacial water structure, and substrate relaxation. Langmuir 28, 8637–8650. https://doi.org/10.1021/la300032h

Li, D., Kaplan, D.I., Knox, A.S., Crapse, K.P., Diprete, D.P., 2014. Aqueous 99Tc, 129I and 137Cs removal from contaminated groundwater and sediments using highly effective low-cost sorbents. J. Environ. Radioact. 136, 56–63. https://doi.org/10.1016/j.jenvrad.2014.05.010

Li, T., Chai, Z., Yang, Z., Xin, Z., Sun, H., Yan, K., 2023. Insights into the influence mechanism of different interlayer cations on the hydration activity of montmorillonite surface: A DFT calculation. Appl. Clay Sci. 239, 106965. https://doi.org/10.1016/j.clay.2023.106965

Li, Y., Han, S., Zhang, B., Tang, H., Han, J., Kang, H., Zhao, Y., Zhu, J., 2022. Nucleation and dissociation of carbon dioxide hydrate in the inter- and intra-particle pores of dioctahedral smectite: Mechanistic insights from molecular dynamics simulations. Appl. Clay Sci. 216, 106344. https://doi.org/10.1016/j.clay.2021.106344

Liu, X., Lu, X., Meijer, E.J., Wang, R., Zhou, H., 2012. Atomic-scale structures of interfaces between phyllosilicate edges and water. Geochim. Cosmochim. Acta 81, 56–68. https://doi.org/10.1016/j.gca.2011.12.009

Martins, D.M.S., Molinari, M., Gonc¸alves, M.A., Mirão, J.P., Parker, S.C., 2014. Toward modeling clay mineral nanoparticles: The edge surfaces of pyrophyllite and their interaction with water. J. Phys. Chem. C 118, 27308–27317. https://doi.org/10.1021/jp5070853

Meena, A.H., Arai, Y., 2017. Environmental geochemistry of technetium. Environ. Chem. Lett. https://doi.org/10.1007/s10311-017-0605-7

Monkhorst, H.J., Pack, J.D., 1976. Special points for Brillouin-zone integrations. Phys. Rev. B 13, 5188–5192. https://doi.org/10.1103/PhysRevB.13.5188

Moore, R.C., Pearce, C.I., Morad, J.W., Chatterjee, S., Levitskaia, T.G., Asmussen, R.M., Lawter, A.R., Neeway, J.J., Qafoku, N.P., Rigali, M.J., Saslow, S.A., Szecsody, J.E., Thallapally, P.K., Wang, G., Freedman, V.L., 2020. Iodine immobilization by materials through sorption and redox-driven processes: A literature review. Sci. Total Environ. 716, 132820. https://doi.org/10.1016/j.scitotenv.2019.06.166

Mousavi, M., Fini, E.H., Hung, A.M., 2019. Underlying Molecular Interactions between Sodium Montmorillonite Clay and Acidic Bitumen. J. Phys. Chem. C 123, 15513–15522. https://doi.org/10.1021/acs.jpcc.9b01960

Neumann, A., Olson, T.L., Scherer, M.M., 2013. Spectroscopic evidence for Fe(II)-Fe(III) electron transfer at clay mineral edge and basal sites. Environ. Sci. Technol. 47, 6969–6977. https://doi.org/10.1021/es304744v

Newton, A.G., Lee, J.Y., Kwon, K.D., 2017. Na-montmorillonite edge structure and surface complexes: An atomistic perspective. Minerals 7. https://doi.org/10.3390/min7050078

Okada, T., Seki, Y., Ogawa, M., 2014. Designed nanostructures of clay for controlled adsorption of organic compounds. J. Nanosci. Nanotechnol. 14, 2121–2134. https://doi.org/10.1166/jnn.2014.8597

Osman, M.A., Ploetze, M., Suter, U.W., 2003. Surface treatment of clay minerals - Thermal stability, basal-plane spacing and surface coverage. J. Mater. Chem. 13, 2359–2366. https://doi.org/10.1039/b302331a

Pedregosa, F., Varoquaux, G., Gramfort, A., Michel, V., Thirion, B., Grisel, O., Blondel, M., Prettenhofer, P., Weiss, R., Dubourg, V., Vanderplas, J., Passos, A., Cournapeau, D., Brucher, M., Perrot, M., Duchesnay, E., 2011. Scikit-learn: Machine Learning in Python Fabian, Journal of Machine Learning Research.

Peng, C., Min, F., Liu, L., Chen, J., 2017. The adsorption of CaOH+ on (001) basal and (010) edge surface of Na-montmorillonite: a DFT study. Surf. Interface Anal. 49, 267–277. https://doi.org/10.1002/sia.6128

Peng, C., Min, F., Liu, L., Chen, J., 2016. A periodic DFT study of adsorption of water on sodium-montmorillonite (001) basal and (010) edge surface. Appl. Surf. Sci. 387, 308–316. https://doi.org/10.1016/j.apsusc.2016.06.079

Perdew, J.P., Burke, K., Ernzerhof, M., 1996. Generalized gradient approximation made simple. Phys. Rev. Lett. 77, 3865–3868. https://doi.org/10.1103/PhysRevLett.77.3865

Ramsay, J.D.F., Swanton, S.W., Bunce, J., 1990. Swelling and dispersion of smectite clay colloids: Determination of structure by neutron diffraction and small-angle neutron scattering. J. Chem. Soc. Faraday Trans. 86, 3919–3926. https://doi.org/10.1039/FT9908603919

Rebitski, E.P., Darder, M., Sainz-Diaz, C.I., Carraro, R., Aranda, P., Ruiz-Hitzky, E., 2020. Theoretical and experimental investigation on the intercalation of metformin into layered clay minerals. Appl. Clay Sci. 186, 105418. https://doi.org/10.1016/j.clay.2019.105418

Sellin, P., Leupin, O.X., 2013. The use of clay as an engineered barrier in radioactive-waste management - A review. Clays Clay Miner. 61, 477–498. https://doi.org/10.1346/CCMN.2013.0610601

Strawn, D.G., Palmer, N.E., Furnare, L.J., Goodell, C., Amonette, J.E., Kukkadapu, R.K., 2004.

Copper sorption mechanisms on smectites. Clays Clay Miner. 52, 321–333. https://doi.org/10.1346/CCMN.2004.0520307

Suter, J.L., Sprik, M., Boek, E.S., 2012. Free energies of absorption of alkali ions onto beidellite and montmorillonite surfaces from constrained molecular dynamics simulations. Geochim. Cosmochim. Acta 91, 109–119. https://doi.org/10.1016/j.gca.2012.04.060

Tazi, S., Rotenberg, B., Salanne, M., Sprik, M., Sulpizi, M., 2012. Absolute acidity of clay edge sites from ab-initio simulations. Geochim. Cosmochim. Acta 94, 1–11. https://doi.org/10.1016/j.gca.2012.07.010

Tong, D., Zhang, Q., Zheng, Y., Caldeira, K., Shearer, C., Hong, C., Qin, Y., Davis, S.J., 2019. Committed emissions from existing energy infrastructure jeopardize 1.5 °C climate target. Nature 572, 373–377. https://doi.org/10.1038/s41586-019-1364-3

Tournassat, C., Bourg, I.C., Holmboe, M., Sposito, G., Steefel, C.I., 2016. Molecular dynamics simulations of anion exclusion in clay interlayer Nanopores. Clays Clay Miner. 64, 374–388. https://doi.org/10.1346/CCMN.2016.0640403

Ulian, G., Moro, D., Valdrè, G., 2021a. DFT simulation of the water molecule interaction with the (00l) surface of montmorillonite. Minerals 11, 501. https://doi.org/10.3390/min11050501

Ulian, G., Moro, D., Valdrè, G., 2021b. Water adsorption behaviour on (001) pyrophyllite surface from ab initio Density Functional Theory simulations. Appl. Clay Sci. 212, 106221. https://doi.org/10.1016/j.clay.2021.106221

Vasconcelos, I.F., Bunker, B.A., Cygan, R.T., 2007. Molecular dynamics modeling of ion adsorption to the basal surfaces of kaolinite. J. Phys. Chem. C 111, 6753–6762. https://doi.org/10.1021/jp065687+

Voora, V.K., Al-Saidi, W.A., Jordan, K.D., 2011. Density functional theory study of pyrophyllite and M-montmorillonites (M = Li, Na, K, Mg, and Ca): Role of dispersion interactions. J. Phys. Chem. A 115, 9695–9703. https://doi.org/10.1021/jp201277f

Wall, N.A., Maulden, E., Gager, E.J., Ta, A.T., Ullberg, R.S., Zeng, G., Nava-Farias, L., Sims, A.P., Nino, J.C., Phillpot, S.R., Szecsody, J.E., Pearce, C.I., 2022. Functionalized Clays for

Radionuclide Sequestration: A Review. ACS Earth Sp. Chem. 6, 2552–2574. https://doi.org/10.1021/acsearthspacechem.2c00098

Wardle, R., Brindley, G.W., 1972. The Crysal Structures of Pyrophyllite, 1Tc, and of Its Dehydroxylate. Am. Mineral. 57, 732–750.

White, G.N., Zelazny, L.W., 1988. Analysis and Implications of the Edge Structure of Dioctahedral Phyllosilicates. Clays Clay Miner. 36, 141–146. https://doi.org/10.1346/CCMN.1988.0360207

Zen, A., Roch, L.M., Cox, S.J., Hu, X.L., Sorella, S., Alfè, D., Michaelides, A., 2016. Toward accurate adsorption energetics on clay surfaces. J. Phys. Chem. C 120, 26402–26413. https://doi.org/10.1021/acs.jpcc.6b09559

Zhao, J., Huang, B.W., Gao, W., Zheng, L.M., Song, P.Z., He, M.C., 2023. Periodic DFT study on heavy metals Cu(II) and Pb(II) atoms adsorption on Na-montmorillonite (010) edge surface. Solid State Commun. 366–367, 115171. https://doi.org/10.1016/j.ssc.2023.115171

Zhu, L., Sheng, D., Xu, C., Dai, X., Silver, M.A., Li, J., Li, P., Wang, Yaxing, Wang, Yanlong, Chen, L., Xiao, C., Chen, J., Zhou, R., Zhang, C., Farha, O.K., Chai, Z., Albrecht-Schmitt, T.E., Wang, S., 2017. Identifying the Recognition Site for Selective Trapping of 99TcO4- in a Hydrolytically Stable and Radiation Resistant Cationic Metal-Organic Framework. J. Am. Chem. Soc. 139, 14873–14876. https://doi.org/10.1021/jacs.7b08632